

Remote epitaxial frustration

Taehwan Jung,¹ Nicholas Hagopian,¹ Anshu Sirohi,¹ Quinn Campbell,² Chengye Dong,³ Zachary T. LaDuca,¹ Tamalika Samanta,¹ Joshua Robinson,^{3,4} Paul M. Voyles,¹ and Jason K. Kawasaki¹

¹*Materials Science and Engineering, University of Wisconsin-Madison, Madison, Wisconsin 53706, United States*

²*Quantum Computer Science Department, Sandia National Laboratories, Albuquerque, New Mexico 87158, United States*

³*Two-dimensional Crystal Consortium, Materials Research Institute,*

Pennsylvania State University, University Park, Pennsylvania 16802, United States

⁴*Department of Materials Science and Engineering, Pennsylvania State University, University Park, Pennsylvania 16802, United States*

(Dated: December 9, 2025)

Remote epitaxy relaxes the constraints of conventional epitaxy, to enable low defect density, chemically abrupt heterostructures and exfoliation of single crystalline membranes. However, definitive evidence for a true remote mechanism remains elusive because most experiments can be explained by alternative mechanism that are macroscopically indistinguishable from true remote epitaxy. Using GdAuGe films grown on graphene/SiC (0001), we present two signatures that cannot be explained by the leading alternatives to the remote mechanism: (1) a few atomic layer thick disordered interlayer at the GdAuGe/graphene interface and (2) a 30° rotated epitaxial relationship between the GdAuGe film and the SiC substrate. Density functional theory calculations indicate these signatures arise from remote epitaxial *frustration*, a competition amongst epitaxy to the remotely screened substrate, to graphene, and to the graphene-induced interfacial reconstruction. Tuning the amplitudes and periodicities of these competing potentials provides new opportunities to intentionally disrupt long-range order.

The formation and structure of condensed matter are typically dominated by short-range nearest neighbor interactions, since atomic orbitals decay exponentially with distance [1]. Usually, it is only when the nearest neighbor interaction strengths are similar, that second nearest neighbor interactions control structure. For example, since hexagonal close packed (hcp) and face centered cubic (fcc) crystals have the same nearest neighbor coordination, the energy difference between second nearest neighbor *ABA* versus *ABC* stacking stabilizes one phase versus the other.

Remote epitaxy flips these energy scales, asserting that in some systems the second nearest neighbor interactions dominate over nearest neighbors. For growth of films on graphene-covered substrates, it has been argued that the “remote” second nearest neighbor interactions between film and substrate, through graphene, are stronger than the “direct” nearest neighbor interactions between film and graphene [2–4]. The resulting film has epitaxial registry to the substrate rather than to the graphene, as if the graphene is transparent. This concept has great utility: insertion of a graphene spacer relaxes the lattice and chemical mismatch constraints of conventional epitaxy, enabling lattice mismatched epitaxy with low dislocation densities [5], atomically abrupt interfaces between chemically dissimilar materials [6], and etch-free exfoliation of single crystalline membranes [2, 3, 7, 8] for applications in heterogeneous integration [9, 10], flexible electronics [2], and new properties induced by large anisotropic strains [11–14].

However, the validity of the remote epitaxy mechanisms remains controversial [15–19]. Model calculations suggest that rather than dominating, the remotely screened electrostatic [3, 15, 20] and covalent/vdW bond-

ing [21] potential fluctuations of most substrates through graphene have similar magnitude or smaller than that of graphene itself (few meV). Moreover, most calculations have ignored graphene-induced interfacial reconstructions to minimize the computational cost [2, 3, 20]. However, such reconstructions are ubiquitous at clean graphene/substrate interfaces, including the $(6\sqrt{3} \times 6\sqrt{3})R30^\circ$ for graphene/SiC (0001) [22], the (6×2) for graphene/Ge (110) [23], and various reconstructions for graphene on metal surfaces [24, 25]. A microscopic theory of remote epitaxy should include these deviations from the bulk-like atomic positions [15].

Experimentally, most observations attributed to remote epitaxy can be explained by alternative mechanisms that are macroscopically indistinguishable from remote epitaxy. Pinhole-seeded epitaxy produces single crystalline films in the same orientation predicted by remote epitaxy, that can also be exfoliated [15, 16]. Pinhole nucleation is likely because most transferred graphene platforms are not clean enough [16, 18]. Thus, open pinholes to the substrate are preferred sites for growth and lateral coalescence of a continuous film [16, 26]. Since most experiments do not quantify the defect density after the critical annealing step that produces pinholes [16], they cannot distinguish between remote and pinhole mechanisms. Moreover, ruling out pinhole seeding by microscopy [27, 28] is challenging because the pinholes are both rare and very small, thus requiring high resolution imaging over prohibitively large areas [15]. Even for nominally pinhole-free graphene/substrate systems, serial direct epitaxy is difficult to rule out. Remote epitaxy has been invoked for AlN films on graphene/SiC (0001) [29]. However, since graphene grows epitaxially to SiC, and AlN grows epitaxially to

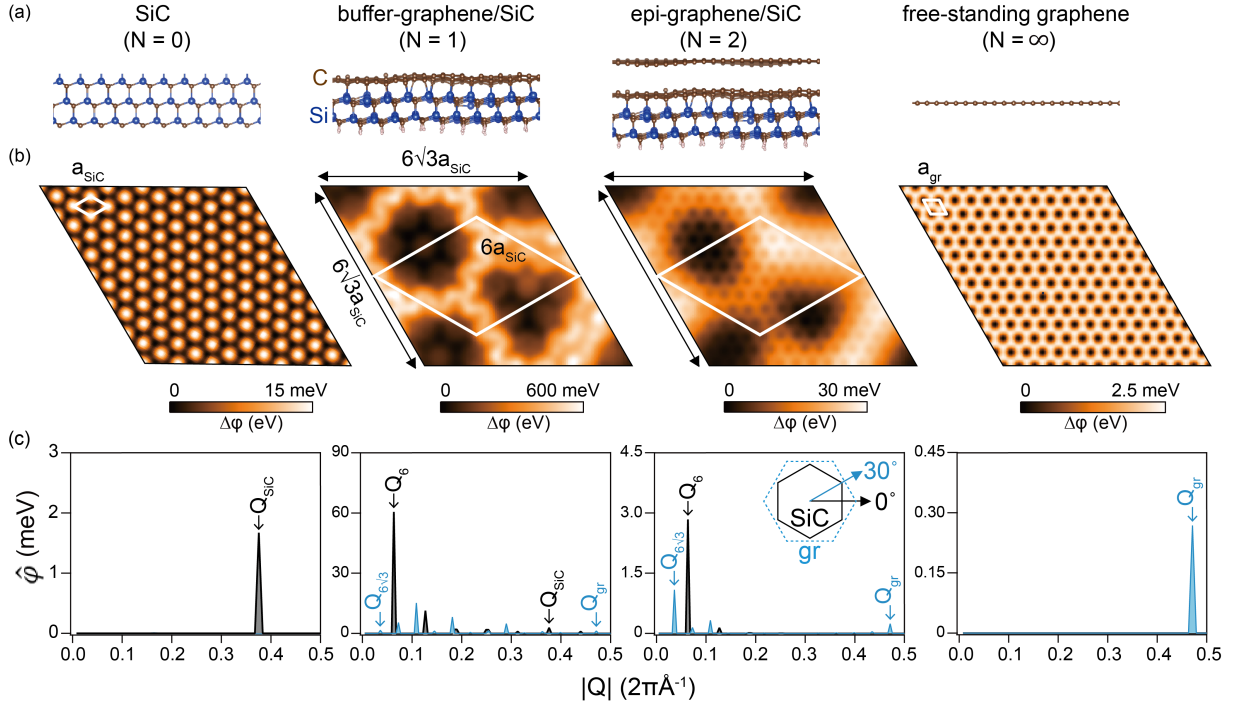


FIG. 1. **Simulations of the remote frustration potentials.** (a) Slab models 6H-SiC (0001), buffer graphene on SiC, epitaxial graphene on SiC, and free-standing graphene. (b) Calculated electrostatic potential φ at 3 Å above each surface. (c) Linecuts through the Fourier transform $\hat{\varphi}(\vec{Q})$, showing single frequencies for bare SiC and freestanding graphene, and multiple peaks above buffer and epitaxial graphene on SiC. The 0° cuts in black are for $\vec{Q} \parallel [11\bar{2}0]_{\text{SiC}}$. The 30° cuts in blue are for $\vec{Q} \parallel [10\bar{1}0]_{\text{SiC}}$.

monolayer graphene, independent of the underlying substrate orientation [30], both direct and remote epitaxy will produce an AlN/graphene/SiC heterostructure with the same long-range orientation.

Here we demonstrate two signatures of remote interactions controlling structure across interfaces that cannot be explained by pinholes or direct interactions. We observe these signatures in a system in which the remote substrate potential, the direct graphene potential, and the potential of a graphene/substrate reconstruction, have similar amplitudes but different periodicities, and thus compete: GdAuGe films grown on clean graphene/6H-SiC (0001). This remote frustration produces two long-range observables, (1) a few atomic layer thick disordered layer at the GdAuGe/graphene/SiC interface, and (2) a 30-degree rotated epitaxial variant, that do not appear for direct epitaxy of GdAuGe on SiC or on isolated graphene. In addition to demonstrating the controlling nature of remote interactions, remote frustration offers opportunities to create new, otherwise inaccessible heterostructures. Tuning the balance of the competing potentials provides a route to engineer novel surface potentials that intentionally disrupt of long-range translational order to stabilize new interfacial glassy phases [31, 32] and quasicrystals, and enable the direct synthesis [33] of twisted Moire matter [34, 35] with intrinsically clean interfaces.

FRUSTRATED SURFACE POTENTIAL

The total potential above a graphene-covered surface contains a direct (nearest neighbor) contribution from graphene φ_{gr} , a remotely screened (second nearest neighbor) contribution from the substrate φ_{sub} , and a contribution from the graphene-induced reconstruction φ_{rec} , each at different amplitudes and periodicities:

$$\varphi_{total} = \varphi_{gr} + T_s \varphi_{sub} + \varphi_{rec}. \quad (1)$$

The first two terms describe the potential in the absence of a reconstruction [21]. $T_s \approx \exp(-k_{TF} \cdot N \Delta z)$ is the free-carrier screening coefficient through metallic graphene, which varies from 0.06 to 0.4 for typical graphene carrier densities 10^{11} to $3 \times 10^{13} \text{ cm}^{-2}$. $1/k_{TF}$ is the screening length, N is the number of graphene layers, and Δz is the thickness of monolayer graphene [21]. Reconstructions are perturbations to the atomic positions in graphene and the substrate at the interface, where $\varphi_{gr} \rightarrow \varphi_{gr} + \varphi'_{gr}$ and $\varphi_{sub} \rightarrow \varphi_{sub} + \varphi'_{sub}$. The reconstruction term is then

$$\varphi_{rec} = \varphi'_{gr} + T_s \varphi'_{sub}. \quad (2)$$

In both Eqs 1 and 2, the terms screened by graphene T_s constitute the remote parts of the potential. Thus, the reconstruction contains a direct part (atomic displacements

within graphene) and a remote part (displacements in the screened substrate beneath graphene).

Van der Waals epitaxy is expected if the graphene potential dominates, $\varphi_{gr} > (T_s\varphi_{sub} + \varphi_{rec})$, resulting in films with out-of-plane orientation that minimize the surface free energy and a weak driving force for in-plane alignment. Remote epitaxy is typically expected for $T_s\varphi_{sub} > \varphi_{gr}$, ignoring the reconstruction φ_{rec} . However, if $T_s\varphi_{sub}$ dominates, the resulting films should mimic the structure of the substrate, making it difficult to distinguish remote epitaxy from pinhole or serial epitaxy.

Here we seek an intermediate condition where two or more potentials have comparable amplitude: $\varphi_{gr} \approx T_s\varphi_{sub} \approx \varphi_{rec}$. In this regime, competing interactions to the substrate, to graphene, and to the long-range reconstructions, each at different periodicities, should create a film that is structurally frustrated, with long-range signatures that are distinct from the simplest remote epitaxy formulation where $T_s\varphi_{sub}$ dominates. Tuning the relative amplitudes of these screened potentials, e.g. by tuning the number of graphene layers N , should tune from direct epitaxy to the substrate ($N = 0$), to remote epitaxial frustration ($N \sim 1$), to vdW epitaxy on graphene ($N \rightarrow \infty$).

Slab density functional theory (DFT) calculations suggest that buffer and epitaxial graphene on 6H-SiC (0001) meet this criteria for tunable frustration. “Buffer” graphene is the first carbon layer that forms on the SiC (0001) surface via Si sublimation (Fig. 1(a)). This layer is buckled from the idealized sp^2 graphene structure ($\Delta z = 0.86$ Å [22]), due to partial covalent bonding to the SiC, and produces a corresponding buckling to the first layer of SiC [36]. “Epitaxial” graphene is the next layer of carbon that forms on top of buffer graphene, and displays smaller distortions ($\Delta z = 0.45$ Å [22]).

Fig. 1(b) shows φ_{total} in the form of computed electrostatic potentials at a distance of $z = 3$ Å above the surface of bare unreconstructed 6H-SiC (0001) ($N = 0$), buffer graphene on SiC ($N = 1$), epitaxial graphene on SiC ($N = 2$), and freestanding graphene ($N \rightarrow \infty$). For bare SiC (0001) and freestanding graphene (0001), φ_{total} follows the periodicities of the SiC and graphene, respectively, and the the resulting Fourier transforms $\hat{\varphi}(\vec{Q})$ have peaks only at multiples of \vec{Q}_{SiC} and \vec{Q}_{gr} , respectively (Fig. 1(c)). See Supplemental Fig 1 for the full two-dimensional Fourier transforms.

In contrast, the electrostatic potential maps above epitaxial and buffer graphene/SiC show complicated patterns with peaks at multiple frequencies, including the graphene lattice (\vec{Q}_{gr}), the SiC lattice (\vec{Q}_{SiC}), the $(6\sqrt{3} \times 6\sqrt{3})R30^\circ$ reconstruction ($\vec{Q}_{6\sqrt{3}}$), and a (6×6) pseudo periodicity (\vec{Q}_6) (Fig. 1(c)). For these surfaces, we predict that the complex spatial structure of φ_{total} will lead to strong geometric frustration of epitaxial crystal layers with suitable lattice mismatch. Supplemental Fig 2, shows that a similar analysis of the covalent/vdW (as

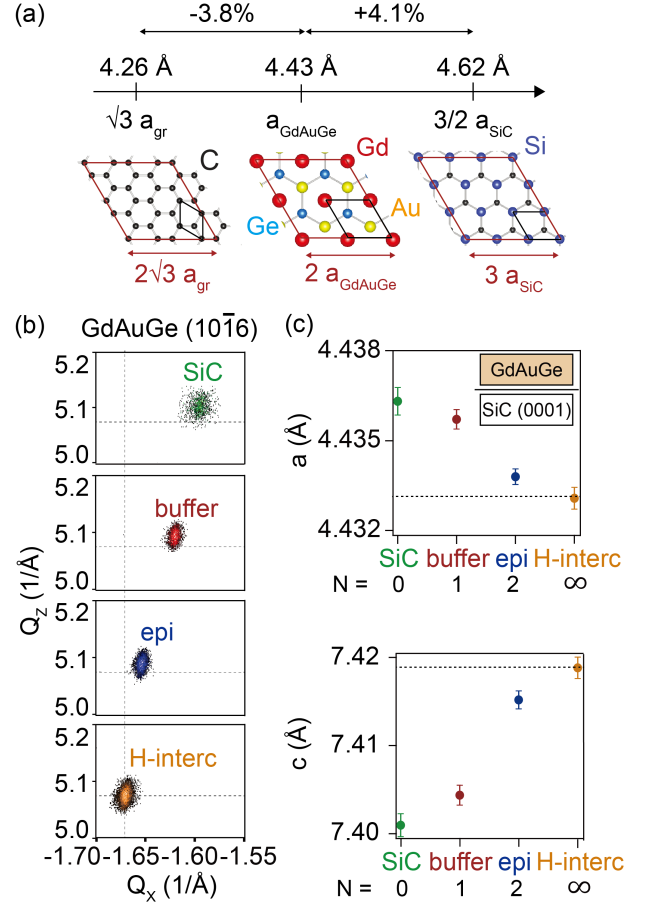


FIG. 2. **Lattice mismatch and strain relaxation for GdAuGe films on graphene/SiC (0001).** (a) Bulk in-plane lattice parameters and expected alignments. The red unit cells outline the smallest commensurate site lattice matching conditions. Black outlines the primitive surface unit cells. (b) Measured reciprocal space maps (RSM) of the GdAuGe 10 $\bar{1}6$ reflection, for 20 nm thick GdAuGe grown on SiC, buffer graphene/SiC, epitaxial graphene/SiC, and H-intercalated graphene on SiC. (c,d) In-plane and out-of-plane lattice parameters of GdAuGe films determined from the RSM. Dotted line represents the bulk lattice parameter.

opposed to electrostatic) potential above graphene also displays multiple competing periodicities.

Fourier analysis clearly distinguishes the remote substrate component $\hat{\varphi}(\vec{Q}_{SiC}) \approx T_s\varphi_{SiC}$ from the direct graphene component $\hat{\varphi}(\vec{Q}_{gr}) \approx \varphi_{gr}$, since they have different frequencies \vec{Q} . However, the reconstruction potential $\varphi_{rec} = \varphi'_{gr} + T_s\varphi'_{SiC}$ has both direct and remote components, at the same frequencies. To distinguish these components, we approximate the direct part of the reconstruction φ'_{gr} by computing the electrostatic potential for a freestanding single graphene layer fixed in the distorted buffer graphene atomic positions (Supplemental Fig 3). For distorted graphene, we find $\varphi'_{gr} \approx \hat{\varphi}(\vec{Q}_6) = 2$ meV, which is a full order of magnitude smaller than $\varphi_{rec} \approx \hat{\varphi}(\vec{Q}_6) = 60$ meV for the full buffer graphene/SiC

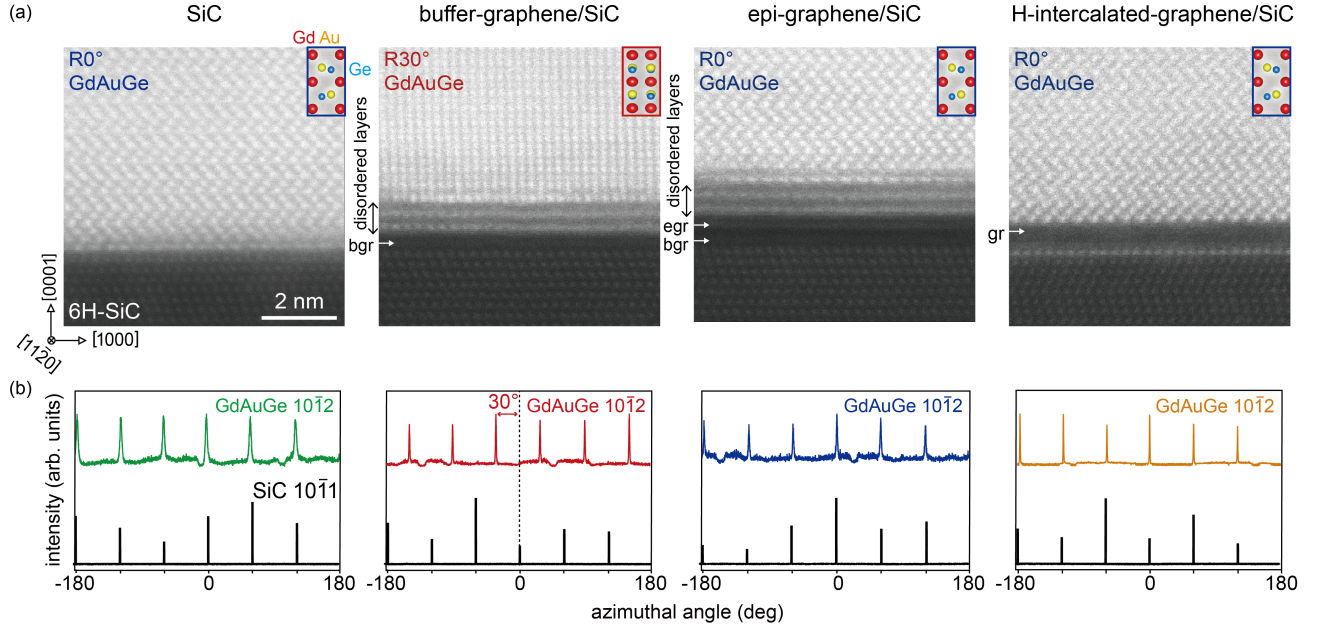


FIG. 3. **Remote frustration of GdAuGe on graphene/SiC.** (a) Cross-sectional HAADF STEM, showing a few atomic layer thick disordered layer at the graphene interface, for GdAuGe on epitaxial graphene (egr) and on buffer graphene (bgr) and a 30° rotated structure for GdAuGe on buffer-graphene. Gd (red), Au (yellow), Ge (blue). (b) X-ray azimuthal scan showing GdAuGe on buffer graphene is rotated in-plane by 30°, and all the other samples are aligned with the SiC.

slab. This suggests that the remote substrate component $T_s\varphi'_{sub}$ plays a dominant role in φ_{rec} for buffer graphene. A similar analysis holds for epitaxial graphene on SiC (Supplemental Fig 4).

OBSERVED FRUSTRATION

To test the remote frustration hypothesis, we select GdAuGe (space group $P6_3mc$) as the film because it has a similar lattice mismatch to graphene (-3.8% for a 30° rotated alignment) and SiC (3.9% to SiC for $2a_{GAG} \approx 3a_{SiC}$), thus maximizing the competition between epitaxy to graphene vs epitaxy to SiC. In contrast, AlN has a much closer lattice match to SiC (-1.3%) than to graphene (-8.7%), and AlN films show no obvious signs of frustration when grown on graphene/SiC [7, 29]. Fig. 2(a) summarizes the lattice parameters and epitaxial alignments expected for direct epitaxy of GdAuGe on SiC (0001) and serial epitaxy on graphene/SiC (0001).

We grew 20 nm thick GdAuGe films on N -layer graphene/6H-SiC (0001) by molecular beam epitaxy (MBE), initiating growth with a 4 nm thick GdAuGe seed layer grown at room temperature to improve wetting on graphene [14], followed by annealing and continued growth at 450°C to a total thickness of 20 nm (Methods). We approximate freestanding graphene ($N = \infty$) with hydrogen-intercalated buffer graphene on SiC. The hydrogen decouples graphene from the SiC substrate [22] (See Methods and Supplemental Fig 5 for graphene characterization). Symmetric $2\theta - \omega$ x-ray diffraction

measurements (Supplemental Fig 6) reveal sharp Kiessig fringes and only the expected 000L reflections with no impurity phases. Reciprocal space maps display a relaxation towards the bulk lattice parameters for increasing N (Fig. 2(b,c)).

Azimuthal X-ray diffraction and cross-section high-angle annular dark field (HAADF) scanning transmission electron microscopy (STEM) (Fig. 3(a,b), Methods) reveal the first long-range signature that is distinct from pinhole or simple serial epitaxy: a 30° in-plane rotation between GdAuGe and SiC on buffer graphene. This rotation does not appear for direct epitaxy of GdAuGe on SiC (0001) or for van der Waals epitaxy of GdAuGe on H-intercalated graphene/SiC. AlN films reported on buffer graphene/SiC (0001) are also unrotated [29].

We hypothesize that the large remote φ_{rec} of buffer graphene / SiC and the screening of φ_{sub} by the single graphene layer create substantial frustration, reducing the energy benefits of aligning the GdAuGe film with the SiC or with graphene. Instead, the system minimizes the strain energy by rotating the GdAuGe by 30 degrees, labeled R30 in Fig 3. Frustration amongst competing graphene, substrate, and reconstruction potentials may also explain the 30° rotation that we previously observed for GdPtSb films grown on graphene/Al₂O₃ (0001) [38].

Large remote φ_{rec} may also be reflected in differences in interfacial bonding for GdAuGe on buffer graphene / SiC compared to GdAuGe on epi graphene or H-intercalated graphene, again leading to R30 domains. Before deposition of GdAuGe, in situ x-ray photoemission spectroscopy (XPS) of the C 1s core level reveals broad

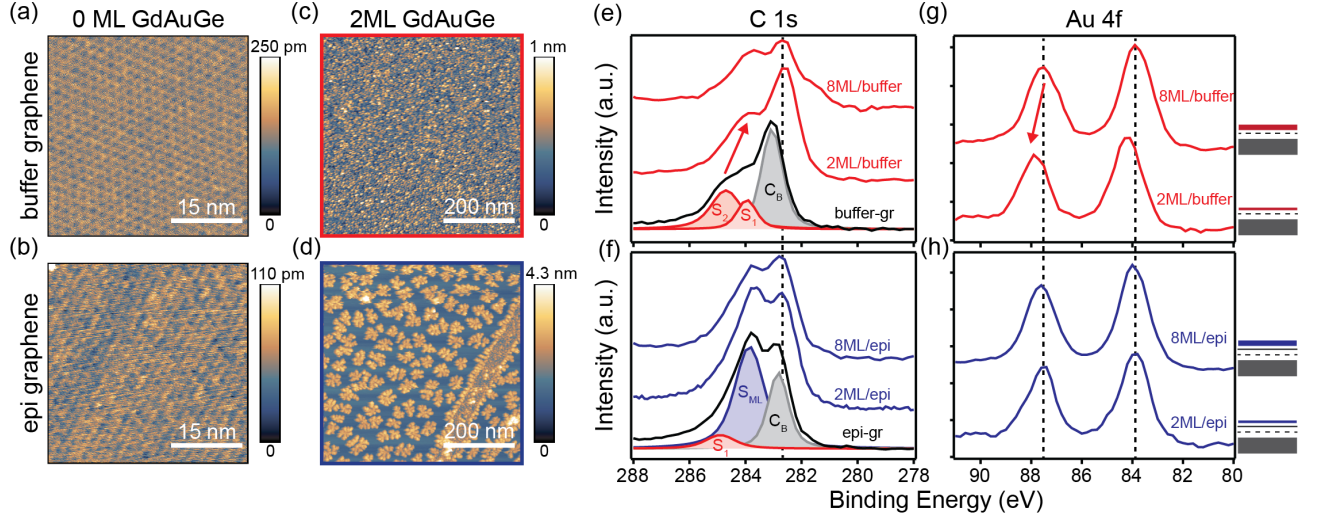


FIG. 4. **Wetting and charge transfer on buffer vs epi graphene/SiC.** (a,b) Filled states STM images of buffer and epi graphene/SiC (0001), respectively, showing the (6×6) quasi periodicity. (c,d) STM images of 2 atomic layers of GdAuGe grown on buffer (filled states) and epi graphene (empty states), respectively, showing smoother wetting on buffer graphene. (e,f) In situ XPS of the C 1s core level for varying thicknesses of GdAuGe grown on buffer and epi graphene. C_B component is from bulk Si-C bonding, $S_{1,2}$ from $sp^2 - sp^3$ buffer graphene, and S_{ML} from sp^2 graphene as identified following Ref. [37]. (g,h) Au 4f core level, showing Au to C charge transfer for GdAuGe on buffer graphene but not on epi graphene.

$S_{1,2}$ components shifted to higher binding energy (Fig. 4(e,black)), consistent with mixed $sp^2 - sp^3$ hybridization [37, 39], compared to the sharp S_{ML} component observed for epi graphene indicative of more sp^2 -like character (Fig. 4(f,black)). After deposition of GdAuGe, we observe core level shifts indicating an Au to C charge transfer across the GdAuGe / buffer graphene interface, that does not appear for GdAuGe / epitaxial graphene. Here we find that deposition of 2 monolayers (ML) GdAuGe on buffer graphene shifts the C 1s to lower binding energy, while the corresponding Au 4f at 2 ML is 1 eV higher in binding energy than the Au 4f for an 8 ML GdAuGe reference sample (Fig. 4(e,g)). No C 1s or Au 4f shifts are observed for growth on epi graphene (Fig. 4(f,h)). In-situ scanning tunneling microscopy (STM) reveals continuous wetting for 2 ML thick GdAuGe films on buffer graphene/SiC, compared to an island morphology on epitaxial graphene/SiC (Fig. 4(c,d)). These observations suggest stronger bonding interactions between GdAuGe and buffer graphene, compared to epitaxial graphene.

Cross sectional STEM reveal a second, striking signature of remote frustration. For films grown on buffer and epitaxial graphene/SiC, the first 2-3 atomic layers of GdAuGe at the graphene interface are highly disordered, in contrast with the crystalline interfaces for direct epitaxy of GdAuGe on SiC or on H-intercalated graphene/SiC (Fig. 3(a)). STEM imaging over larger areas confirms this disordered interface is ubiquitous, although not uniformly disordered everywhere (Supplemental Fig 7). We interpret these frustrated layers to arise from the competition between epitaxy of the GdAuGe film to the graphene, SiC, and reconstruction potentials, each at different periodicity. Both the

relative amplitudes of these potentials and their lattice mismatches to the film (periodicities) appear to be important, since the frustrated interface appears for GdAuGe films which have nearly equal lattice mismatch to graphene and to SiC, whereas AlN films that are nearly lattice matched to SiC do not display the disordered interface.

In Fig. 5 we track the formation of the disordered interfacial layers as a function of annealing, starting from a 4 nm thick GdAuGe room temperature seed layer on buffer graphene/SiC. We observe two distinct transitions. The first transition at $\sim 200^\circ\text{C}$ is solid phase epitaxy of GdAuGe, which converts the mostly amorphous seed to a strained crystalline film with a crystalline interface. This transition is marked by a change from a diffuse and slightly spotty reflection high energy electron diffraction (RHEED) pattern to a streaky pattern. We quantify the onset of surface crystallization via the normalized RHEED intensity (Fig. 5(c) and Supplemental Fig. 8). Cross sectional STEM more clearly resolves this transition: the GdAuGe seed layer is mostly amorphous (Fig. 5(a,upper)) with a occasional few nanometer diameter crystallites (Supplemental Fig 9). A 360°C anneal crystallizes the entire 4 nm thick layer, but does not form the disordered interface (Fig. 5(a)). This solid phase epitaxy (SPE) of GdAuGe is also marked by an amorphous to crystalline densification: XRD for the room temperature seed shows a weak peak near the bulk 0004 reflection, which shifts towards higher angle after the anneal at 360°C . The resulting film is under $\varepsilon_{zz} \sim 0.8\%$ strain.

Annealing to 450°C produces the second transition: appearance of the disordered interlayer observed by STEM, and a relaxation to near the bulk lattice param-

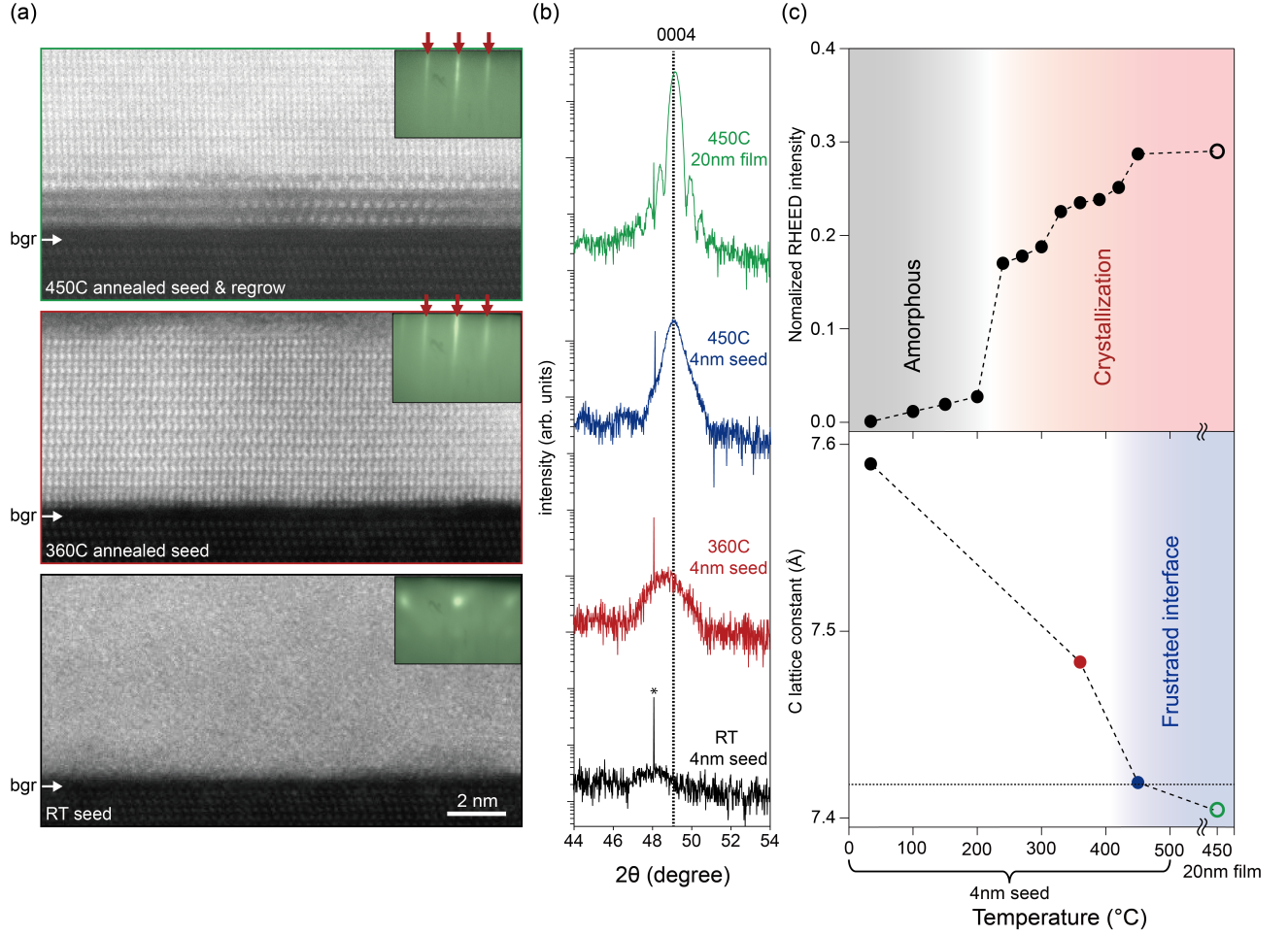


FIG. 5. **Formation of the frustrated interface.** (a) STEM images of a 4 nm thick GdAuGe seed layer on buffer graphene/SiC as a function of anneal temperature. The buffer graphene layer is noted by the white arrow. The corresponding RHEED patterns are shown in the insets, where red arrows mark the crystalline reflections. (b) X-ray diffraction around the 0004 reflection. (c) Normalized RHEED intensity ($I_{\text{diffracted}}/I_{\text{background}}$) and c lattice parameter from x-ray diffraction, as function of anneal temperature. The bulk lattice parameter is marked by the dotted line.

ter by XRD. Notably, this relaxation is not thickness-induced: a 4 nm thick seed annealed to 450°C displays nearly the same lattice parameter as a film annealed at 450°C and grown to a total thickness of 20 nm (Fig. 5(b,c)). This suggests that strain across the GdAuGe/graphene interface may play an important role in the formation of the disordered interlayer. Such a strain relaxation is expected within the frustration picture: the competing mismatch of GdAuGe to SiC, graphene, and the reconstruction would produce a complex evolution of the GdAuGe film lattice parameter. At the interface between crystalline GdAuGe and disordered GdAuGe, we also observe reconstruction with $3\times$ lateral periodicity, which may be an additional mechanism to relax the strain across the GdAuGe / buffer graphene interface. A similar strain evolution appears upon annealing of a GdAuGe seed layer on epitaxial graphene / SiC (Supplemental Fig. 10).

DISCUSSION

Our combined analytical model, DFT calculations, and experiments display two signatures of structural frustration in GdAuGe films on buffer and epi graphene/SiC: a rotated epitaxial alignment and a few-monolayer thick disordered interface. These signature are inconsistent with pinhole epitaxy or direct serial epitaxy, the leading alternate explanations to remote epitaxy. Therefore, these results provide strong, structurally distinct, evidence for the importance of remote interactions, screened by graphene, in epitaxial growth of GdAuGe on buffer and epitaxial graphene on SiC.

Our experiments and theory also suggest a prominent role for the remote interactions with graphene-induced reconstructions of the SiC substrate. The reconstruction is the major contribution to the computed electrostatic potential above buffer and epi graphene/SiC (Fig. 1), and produces changes to the bonding and wetting

across GdAuGe/graphene/SiC interfaces (Fig. 4). The disordered GdAuGe interface on epitaxial graphene has distinctly remote character. φ'_{gr} in epitaxial graphene is negligible compared to that of buffer graphene, yet the disordered interface layers persist. Decoupling the graphene from the SiC substrate via H intercalation has the combined effect of suppressing the reconstruction ($\varphi_{rec} \rightarrow 0$) and attenuating the substrate ($T_s\varphi_{SiC} \rightarrow 0$). Both factors favor simple direct vdW epitaxy of GdAuGe in an R0 orientation and without a disordered interface, exactly as observed.

For growth on buffer graphene the observed charge transfer and wetting are consistent with both direct and remote interactions. In a direct picture, distortions in graphene towards more sp^3 -like character are expected to enhance wetting and promote bond formation with a film that may not occur for pristine graphene. However, remote interactions are also expected to enhance charge transfer and wetting. Remote interactions through graphene have previously been invoked to explain the wetting of liquids on graphene-covered surfaces as a function of number of graphene layers [40], although this interpretation has remained controversial [41]. Our DFT calculations suggest that remotely screened substrate distortions are the dominant contribution (Supplemental Fig 3), supporting the remote picture. Further experiments and theory are required to more rigorously quantify the remote vs direct contributions to bonding across reconstructed graphene-covered surfaces, and their impacts on epitaxial alignment, disordered layer formation, and strain relaxation.

Remote epitaxial frustration provides a new avenue to design surface potentials that intentionally break long-range translational order in a film. These new degrees of freedom have the potential to result in new interfacial structures and straightforward synthesis of otherwise inaccessible heterostructures. An advantage of graphene-covered substrates, compared with other methods to engineer surfaces, is that that graphene passivates the surface [42, 43] making its atomic-scale structure more robust to surface adsorbates (and thus easier to design). Moreover, the graphene enables the relative amplitudes of the graphene, substrate, and reconstruction potentials to be tuned via (gate-induced) screening (Eq 1). Similar frustration may be able to stabilize new interfacial quasicrystals, or even achieve the grand challenge in glass physics controlling short and medium-range ordering and synthesizing an “ideal” glass via geometric frustration [44] created with substrates with interactions at competing length scales. Finally, the graphene-induced twist angle provides a new route towards direct synthesis of

twisted Moire heterostructures without exfoliation and layer stacking and with intrinsically clean interfaces.

ACKNOWLEDGMENT

This work was primarily supported by the U.S. Department of Energy, Office of Science, Basic Energy Sciences, under award no. DE-SC0023958 (GdAuGe synthesis, STM, and XPS by T.J., A.S., J.K.K.). Additional support came from the Air Force Office of Scientific Research FA9550-21-0127 (film characterization by Z.L., J.K.K.) and from the NSF through the University of Wisconsin Materials Research Science and Engineering Center under Grant No. NSF DMR-2309000 (film characterization by N.H., T.S., J.K.K., and PMV). We acknowledge the use of facilities and instrumentation in the Wisconsin Center for Nanoscale Technology. This Center is partially supported by the Wisconsin Materials Research Science and Engineering Center (NSF DMR-2309000) and by the University of Wisconsin–Madison.

Graphene on SiC samples for this publication were provided by The Pennsylvania State University Two-Dimensional Crystal Consortium – Materials Innovation Platform (2DCC-MIP) which is supported by NSF cooperative agreement DMR-2039351 (C.D. and J.S.).

QTC is supported by the by the Laboratory Directed Research and Development (LDRD) program at Sandia National Laboratories under project 233271. This work was performed, in part, at the Center for Integrated Nanotechnologies, an Office of Science User Facility operated for the U.S. Department of Energy (DOE) Office of Science. Sandia National Laboratories is a multi-mission laboratory managed and operated by National Technology & Engineering Solutions of Sandia, LLC (NTESS), a wholly owned subsidiary of Honeywell International Inc., for the U.S. Department of Energy’s National Nuclear Security Administration (DOE/NNSA) under contract DE-NA0003525. This written work is authored by an employee of NTESS. The employee, not NTESS, owns the right, title and interest in and to the written work and is responsible for its contents. Any subjective views or opinions that might be expressed in the written work do not necessarily represent the views of the U.S. Government. The publisher acknowledges that the U.S. Government retains a non-exclusive, paid-up, irrevocable, world-wide license to publish or reproduce the published form of this written work or allow others to do so, for U.S. Government purposes. The DOE will provide public access to results of federally sponsored research in accordance with the DOE Public Access Plan.

[1] L. Pauling, *The nature of the chemical bond and the structure of molecules and crystals: an introduction to modern structural chemistry*, vol. 18 (Cornell university

press, 1960).

[2] Y. Kim, S. S. Cruz, K. Lee, B. O. Alawode, C. Choi, Y. Song, J. M. Johnson, C. Heidelberg, W. Kong,

- S. Choi, et al., Nature **544**, 340 (2017).
- [3] W. Kong, H. Li, K. Qiao, Y. Kim, K. Lee, Y. Nie, D. Lee, T. Osadchy, R. J. Molnar, D. K. Gaskill, et al., Nature materials **17**, 999 (2018).
 - [4] J. Jiang, X. Sun, X. Chen, B. Wang, Z. Chen, Y. Hu, Y. Guo, L. Zhang, Y. Ma, L. Gao, et al., Nature communications **10**, 4145 (2019).
 - [5] S.-H. Bae, K. Lu, Y. Han, S. Kim, K. Qiao, C. Choi, Y. Nie, H. Kim, H. S. Kum, P. Chen, et al., Nature nanotechnology **15**, 272 (2020).
 - [6] M. S. S. V. S. K. A. M. S. K. J. K. Strohbeen, Patrick J., ACS Appl. Mater. Interfaces **13**, eadj5379 (2021), URL <https://doi.org/10.1021/acsami.1c10701>.
 - [7] J. Kim, C. Bayram, H. Park, C.-W. Cheng, C. Dimitrakopoulos, J. A. Ott, K. B. Reuter, S. W. Bedell, and D. K. Sadana, Nature communications **5**, 4836 (2014).
 - [8] H. Yoon, T. K. Truttman, F. Liu, B. E. Matthews, S. Choo, Q. Su, V. Saraswat, S. Manzo, M. S. Arnold, M. E. Bowden, et al., Science Advances **8**, eadd5328 (2022).
 - [9] J. Shin, H. Kim, S. Sundaram, J. Jeong, B.-I. Park, C. S. Chang, J. Choi, T. Kim, M. Saravanapavanantham, K. Lu, et al., Nature **614**, 81 (2023).
 - [10] M. Yuan, J. Feng, H. Li, H. Gao, Y. Qiu, L. Jiang, and Y. Wu, Nature Nanotechnology **20**, 381 (2025).
 - [11] D. Du, S. Manzo, C. Zhang, V. Saraswat, K. T. Genser, K. M. Rabe, P. M. Voyles, M. S. Arnold, and J. K. Kawasaki, Nature communications **12**, 2494 (2021).
 - [12] D. Du, J. Hu, and J. K. Kawasaki, Applied Physics Letters **122** (2023).
 - [13] Z. LaDuca, K. Su, S. Manzo, M. S. Arnold, and J. K. Kawasaki, Physical Review Materials **7**, 083401 (2023).
 - [14] Z. LaDuca, T. Samanta, N. Hagopian, T. Jung, K. Su, K. Genser, K. M. Rabe, P. M. Voyles, M. S. Arnold, and J. K. Kawasaki, Nano Letters **24**, 10284 (2024).
 - [15] Z. LaDuca, A. Sirohi, Q. Campbell, and J. K. Kawasaki, 2D Materials **12**, 043006 (2025).
 - [16] S. Manzo, P. J. Strohbeen, Z. H. Lim, V. Saraswat, D. Du, S. Xu, N. Pokharel, L. J. Mawst, M. S. Arnold, and J. K. Kawasaki, Nature communications **13**, 4014 (2022).
 - [17] D. Jang, C. Ahn, Y. Lee, S. Lee, H. Lee, D. Kim, Y. Kim, J.-Y. Park, Y.-K. Kwon, J. Choi, et al., Advanced Materials Interfaces **10**, 2201406 (2023).
 - [18] M. Zulqurnain, O. J. Burton, M. Al-Hada, L. E. Goff, S. Hofmann, and L. C. Hirst, Nanotechnology **33**, 485603 (2022).
 - [19] X. Yan, H. Cao, Y. Li, H. Hong, D. J. Gosztola, N. P. Guisinger, H. Zhou, and D. D. Fong, APL Materials **10** (2022).
 - [20] L. Dai, J. Zhao, J. Li, B. Chen, S. Zhai, Z. Xue, Z. Di, B. Feng, Y. Sun, Y. Luo, et al., Nature Communications **13**, 2990 (2022).
 - [21] J. K. Kawasaki and Q. T. Campbell, *An analytical model for the remote epitaxial potential* (2025), 2507.09913, URL <https://arxiv.org/abs/2507.09913>.
 - [22] J. Sforzini, L. Nemec, T. Denig, B. Stadtmüller, T.-L. Lee, C. Kumpf, S. Soubatch, U. Starke, P. Rinke, V. Blum, et al., Physical review letters **114**, 106804 (2015).
 - [23] B. Kiraly, R. M. Jacobberger, A. J. Mannix, G. P. Campbell, M. J. Bedzyk, M. S. Arnold, M. C. Hersam, and N. P. Guisinger, Nano Letters **15**, 7414 (2015), pMID: 26506006, <https://doi.org/10.1021/acs.nanolett.5b02833>, URL <https://doi.org/10.1021/acs.nanolett.5b02833>.
 - [24] A. T. N'Diaye, S. Bleikamp, P. J. Feibelman, and T. Michely, Phys. Rev. Lett. **97**, 215501 (2006), URL <https://link.aps.org/doi/10.1103/PhysRevLett.97.215501>.
 - [25] S. K. Hämäläinen, M. P. Boneschanscher, P. H. Jacobse, I. Swart, K. Pussi, W. Moritz, J. Lahtinen, P. Liljeroth, and J. Sainio, Phys. Rev. B **88**, 201406 (2013), URL <https://link.aps.org/doi/10.1103/PhysRevB.88.201406>.
 - [26] Z. H. Lim, S. Manzo, P. J. Strohbeen, V. Saraswat, M. S. Arnold, and J. K. Kawasaki, Applied Physics Letters **120** (2022).
 - [27] C. S. Chang, K. S. Kim, B.-I. Park, J. Choi, H. Kim, J. Jeong, M. Barone, N. Parker, S. Lee, X. Zhang, et al., Science Advances **9**, eadj5379 (2023).
 - [28] R. Jia, Y. Xin, M. Potter, J. Jiang, Z. Wang, H. Ma, Z. Zhang, Z. Liang, L. Zhang, Z. Lu, et al., Nature pp. 1–8 (2025).
 - [29] K. Qiao, Y. Liu, C. Kim, R. J. Molnar, T. Osadchy, W. Li, X. Sun, H. Li, R. L. Myers-Ward, D. Lee, et al., Nano letters **21**, 4013 (2021).
 - [30] F. Liu, T. Wang, X. Gao, H. Yang, Z. Zhang, Y. Guo, Y. Yuan, Z. Huang, J. Tang, B. Sheng, et al., Science Advances **9**, ead8484 (2023).
 - [31] S. F. Swallen, K. L. Kearns, M. K. Mapes, Y. S. Kim, R. J. McMahon, M. D. Ediger, T. Wu, L. Yu, and S. Satija, Science **315**, 353 (2007).
 - [32] M. D. Ediger, The Journal of chemical physics **147** (2017).
 - [33] M. Fortin-Deschenes, K. Watanabe, T. Taniguchi, and F. Xia, Nature Materials **23**, 339 (2024).
 - [34] Y. Cao, V. Fatemi, S. Fang, K. Watanabe, T. Taniguchi, E. Kaxiras, and P. Jarillo-Herrero, Nature **556**, 43 (2018).
 - [35] S. F. Zhao, X. Cui, P. A. Volkov, H. Yoo, S. Lee, J. A. Gardener, A. J. Akey, R. Engelke, Y. Ronen, R. Zhong, et al., Science **382**, 1422 (2023).
 - [36] M. Conrad, J. Rault, Y. Utsumi, Y. Garreau, A. Vlad, A. Coati, J.-P. Rueff, P. F. Miceli, and E. H. Conrad, Phys. Rev. B **96**, 195304 (2017), URL <https://link.aps.org/doi/10.1103/PhysRevB.96.195304>.
 - [37] M. Conrad, J. Rault, Y. Utsumi, Y. Garreau, A. Vlad, A. Coati, J.-P. Rueff, P. Miceli, and E. Conrad, Physical Review B **96**, 195304 (2017).
 - [38] D. Du, T. Jung, S. Manzo, Z. LaDuca, X. Zheng, K. Su, V. Saraswat, J. McChesney, M. S. Arnold, and J. K. Kawasaki, Nano Letters **22**, 8647 (2022).
 - [39] K. Emtsev, F. Speck, T. Seyller, L. Ley, and J. D. Riley, Physical Review B—Condensed Matter and Materials Physics **77**, 155303 (2008).
 - [40] J. Rafiee, X. Mi, H. Gullapalli, A. V. Thomas, F. Yavari, Y. Shi, P. M. Ajayan, and N. A. Koratkar, Nature materials **11**, 217 (2012).
 - [41] C.-J. Shih, Q. H. Wang, S. Lin, K.-C. Park, Z. Jin, M. S. Strano, and D. Blankschtein, Physical review letters **109**, 176101 (2012).
 - [42] N. Briggs, B. Bersch, Y. Wang, J. Jiang, R. J. Koch, N. Nayir, K. Wang, M. Kolmer, W. Ko, A. De La Fuente Duran, et al., Nature materials **19**, 637 (2020).
 - [43] R. Jacobberger, S. Roy, V. Mangu, M. Arnold, F. Cavallo, M. Lagally, et al., ACS Applied Materials & Interfaces **9**, 17629 (2017).

- [44] D. R. Nelson and F. Spaepen, Solid State Physics **42**, 1 (1989).
- [45] P. Giannozzi, S. Baroni, N. Bonini, M. Calandra, R. Car, C. Cavazzoni, D. Ceresoli, G. L. Chiarotti, M. Cococcioni, I. Dabo, et al., Journal of physics: Condensed matter **21**, 395502 (2009).
- [46] M. J. van Setten, M. Giantomassi, E. Bousquet, M. J. Verstraete, D. R. Hamann, X. Gonze, and G.-M. Rignanese, Computer Physics Communications **226**, 39 (2018).
- [47] J. P. Perdew, K. Burke, and M. Ernzerhof, Physical review letters **77**, 3865 (1996).
- [48] H. J. Monkhorst and J. D. Pack, Physical review B **13**, 5188 (1976).

ONLINE METHODS

A. Graphene growth on SiC.

Different types of graphene were synthesized on the Si-face of 6H-SiC substrates (Coherent Inc.) via thermal decomposition. The SiC substrates were first annealed at 1400°C and 700 Torr in a 10 % H_2 /Ar mixture for 30 min to remove surface contamination. Subsequently, the samples were annealed in pure Ar at 1600°C and 700 Torr for 30 min to form the buffer layer, and at 1800°C and 700 Torr for 20 min to produce monolayer epitaxial graphene, respectively. Quasi-freestanding monolayer graphene was prepared by hydrogen intercalation of buffer layer at 700°C and 600 Torr in pure H_2 for 30 min. Raman spectroscopy is performed in a Horiba LabRam Raman system with a 532 nm laser and a 600 grooves cm^{-1} grating. The spectra are obtained with a power of 6 mW and an integration time of 15 s. Atomic force microscopy (AFM) is performed using Bruker Dimension Icon instrument equipped with a ScanAsyst-Air ($k = 0.4$ N/m) tip in tapping mode.

B. MBE growth of GdAuGe.

GdAuGe films were synthesized by molecular beam epitaxy (MBE) on various graphene/6H-SiC(0001) substrates, including bare SiC, buffer graphene/SiC, epi graphene/SiC, and hydrogen-intercalated graphene/SiC. Hexagonal GdAuGe films with the $P6_3mc$ crystal structure were grown via co-deposition of elemental Gd, Au, and Ge sources. A 5 nm-thick seed layer was deposited at room temperature, followed by continued growth to achieve a total film thickness of approximately 20 nm. The deposition process followed protocols similar to those reported in [14]. Elemental fluxes were monitored using a quartz crystal microbalance and further calibrated through Rutherford backscattering spectrometry (RBS) on dedicated calibration samples.

C. in situ STM and XPS.

Samples were transferred from the MBE to a combined STM (scanning tunneling microscopy) and XPS (x-ray photoemission spectroscopy) system via an ultrahigh vacuum manifold. STM measurements were performed at room temperature using an Omicron VT-STM with PtIr tips. XPS measurements were performed at room temperature using an Omicron EA125 analyzer and an un-monochromated Mg $K\alpha$ x-ray source. The Fermi energy was calibrated using a gold film that is in electrical contact with the sample.

D. X-ray diffraction.

Structural analysis of the films was carried out using a Malvern Panalytical Empyrean X-ray diffractometer equipped with a four-circle goniometer and a z-translation sample stage. Symmetric $2\theta - \omega$ scans were performed to evaluate the out-of-plane lattice orientation and phase purity. Azimuthal pole figure measurements were employed to determine the in-plane epitaxial relationship between the film and substrate. Reciprocal space maps (RSMs) around asymmetric reflections were collected to assess lattice relaxation and strain state. All measurements were conducted using Cu $K\alpha$ radiation ($\lambda = 1.5406$ Å) operating at 45 kV and 40 mA.

E. STEM.

Cross-section lift-outs were prepared with a 30 kV Xe plasma focused ion beam (PFIB, FEI Helios) or a 30 kV Ga FIB (Zeiss Auriga). Thinning of the cross section to electron transparency was performed with the Ga FIB, with rough shaping performed at 30 kV, stepping down in voltage until a final polishing step at 2 kV. As needed, an Ar ion mill (Fischione 1040 Nanomill) was operated at 800 eV to thin cross-sections further and remove FIB surface damage and artifacts. Samples were plasma cleaned with air intake gas at 18 W for 5 m in an IBSS group MCA to remove contamination prior to STEM characterization.

Atomic resolution imaging was performed with a CEOS probe-corrected Thermo-Fisher Titan scanning transmission electron microscope (STEM). The STEM was operated at 200 kV with spot size 10 and a 70 $\mu m/23.3$ mrad aperture, corresponding to a beam current of 22.3 pA. Imaging was conducted with a high angle annular dark field (HAADF) detector at a camera length of 160 mm corresponding to detection angles between 54 to 270 mrad.

F. Computational Details.

We created a SiC $(6\sqrt{3} \times 6\sqrt{3})R30^\circ$ slab, and bulk SiC slab model where the bottom layers of the substrate were terminated with passivating hydrogen and the top layers were either exposed to vacuum or connected with a buffer graphene or epitaxial graphene layer. In our pure graphene slab model, we only include one layer of graphene with no passivation. 20 Å of vacuum region was placed between the ends to avoid unphysical interaction

between the two surfaces.

Electronic structure calculations are done using the QUANTUM ESPRESSO package [45]. We use norm-conserving pseudopotentials from the PseudoDojo repository [46] and the Perdew-Burke-Ernzerhof exchange-correlation functional [47]. We use kinetic energy cutoffs of 50 Ry and 400 Ry for the plane wave basis sets used to describe the Kohn-Sham orbitals and charge density, respectively. We use a $2 \times 2 \times 1$ Monkhorst-Pack grid [48] to sample the Brillouin zone in our calculations.